Journal of Hazardous Materials 180 (2010) 234–240

Contents lists available at ScienceDirect

Journal of Hazardous Materials

journal homepage: www.elsevier.com/locate/jhazmat

Nanoporous manganese oxides as environmental protective materials—Effect of Ca and Mg on metals sorption

Jouni Pakarinen [a,*], Risto Koivula [b], Markku Laatikainen [a], Katri Laatikainen [a], Erkki Paatero [a], Risto Harjula [b]

[a] Lappeenranta University of Technology, Laboratory of Industrial Chemistry, P.O.Box 20, FI-53851 Lappeenranta, Finland
[b] University of Helsinki, Laboratory of Radiochemistry, P.O.Box 55, FI-00014, Helsinki, Finland

ARTICLE INFO

Article history:
Received 14 December 2009
Received in revised form 16 March 2010
Accepted 6 April 2010
Available online 13 April 2010

Keywords:
Ion exchange
Manganese oxide
OMS
Molecular sieve
Diffusion

ABSTRACT

The selectivity of nanoporous manganese oxides for some alkali and transition metals over calcium and magnesium was studied. Two tunnel-structured oxides (OMS-1 and OMS-2) were synthesized by means of a hydrothermal route. Competitive uptake of metals and acid was studied using batch kinetic measurements at different metal ion concentrations. The experimental data were correlated with a dynamic model. The results show that the studied OMS materials selectively adsorb Cu, Ni and Cd in the presence of Ca and Mg. It was also found that the exchange rates were reasonably high due to the small particle dimensions. Both materials are stable in the studied conditions and their maximum Cu uptake capacity was 0.9–1.3 mmol/g. The results indicate that both materials have potential for environmental applications involving the uptake of harmful metal ions.

1. Introduction

With increased concern about the environment, attempts are being made to minimize the impact on the natural world of various industrial operations. Worldwide, mining operations handle several million tons of metal solutions annually and sometimes environmental damage occurs as a result of leaks in solution handling or poor tailings management. The consequences for the local population and surrounding ecosystem can be catastrophic, as reviewed by Johnson and Hallberg [1].

Bentonite is conventionally used as a protective material around places where different chemicals are transported or handled [2,3]. Fall et al. [4] and Eren et al. [5,6] have studied the utilization of bentonite or manganese oxide-coated bentonite in the uptake of heavy metals. However, materials specifically designed to protect mining areas or bedrock do not exist. Inexpensive and stable materials which adsorb heavy metals or radio nuclides and which are non-selective for alkaline earth metals (Ca and Mg) present in ground waters are thus needed.

Octahedrally ordered nanoporous manganese oxides play an important role in natural soil and aquatic systems and a large number of studies to synthesize and characterize these materials have been carried out [e.g. [7–9]]. The synthesized materials are built of Mn(IV) ions coordinated octahedrally by oxygen atoms. The octahedra share edges and/or corners and form various tunnel or layered structures [9], which are called octahedral molecular sieves (OMS). The three-dimensional pore structures of OMS-1 and OMS-2 are shown in Fig. 1. Mg^{2+} and K^{+} are the template ions used in the synthesis. The size of the tunnels in 3×3 OMS-1 and in 2×2 OMS-2 is about 0.7 and 0.46 nm, respectively [9]. The corresponding natural minerals are known as todorokite and hollandite (cryptomelane in K-form).

Due to the presence of Mn^{3+} and Mn^{2+}, and vacant octahedra in the MnO_2 structure, the OMS materials act as cation exchangers. Selective uptake of heavy metals with OMS materials has been extensively studied [10–15] and they have been shown to have strong affinity for several transition metals and radio nuclides [16,17].

In this study the metal-adsorbing properties of OMS-1 and OMS-2, which can be prepared using inexpensive hydrometallurgical side-streams [18], were utilized in removal of environmentally hazardous elements. In view of interest in their utilization in mining operations and other environmental applications, the materials were assessed for their heavy metal capturing ability. One particular objective was to investigate the interfering action of Ca and Mg, which are always present in process and natural waters and can severely consume the capacity of the adsorption material.

This paper thus deals with the synthesis of two OMS materials, and their characterization and use in metals sorption at different Ca and Mg concentrations (also Li and K for OMS-2). The ion exchange

* Corresponding author. Fax: +358 5 6212199.
E-mail address: Jouni.Pakarinen@lut.fi (J. Pakarinen).

0304-3894/$ – see front matter © 2010 Elsevier B.V. All rights reserved.
doi:10.1016/j.jhazmat.2010.04.019

Nomenclature

List of symbols

A^+	univalent counter-ion
b_m	mass transport parameter, 1/s
c	concentration, mol/L
d	average diameter of OMS crystals, m
D_m	micro-crystalline diffusion coefficient, m^2/s
D_{ax}	axial dispersion coefficient, m^2/s
F	Faraday constant
h_i	empirical parameter in Eq. (1)
I	ionic strength, mol/L
J	ion flux, mol/(m^2 s)
k_{dis}	rate constant of the disproportionation reaction, mol/(L s)
K_{dis}	equilibrium constant of the disproportionation reaction
L	average length of the OMS crystals, m
m	potential parameter in Eq. (3)
N	number of cations
p	heterogeneity parameter in Eq. (1)
q	amount of adsorbate in the solid phase, mol/kg
q_{max}	total amount of ion exchange sites, mol/kg
r_{dis}	rate of the disproportionation reaction, mol/(L s)
R	gas constant, 8.314 J/(mol K)
t	time, s
T	temperature, K or °C
u	interstitial velocity, m/s
V	volume, L
x	axial coordinate, m
y	diffusion coordinate, m
z	ion charge
□	empty vacant site

Greek letters

α, β, γ	reaction orders in Eq. (4)
κ	affinity constant, L/mol
ρ	density, kg/L
φ	electric potential, V
ν	stoichiometric coefficient

Subscripts and superscripts

b	non-specific binding
feed	feed value
H	proton
i, j	ion
init	initial value
liq	liquid phase
s	solid phase
sp	specific binding
0	initial value
e, f, r	disproportionation coefficients

equilibria were modelled using the NICA (non-ideal competitive adsorption) [19] isotherm and mass transport in the nanoporous crystals was calculated using the Nernst–Planck equation. In addition to the ion exchange at the tunnel sites, reactions involving the Mn framework were also taken into account.

2. Theory

2.1. Equilibrium binding model

Modelling of metal sorption from the solution to the solid OMS phase is explained in an earlier article [20]. In brief, metal binding

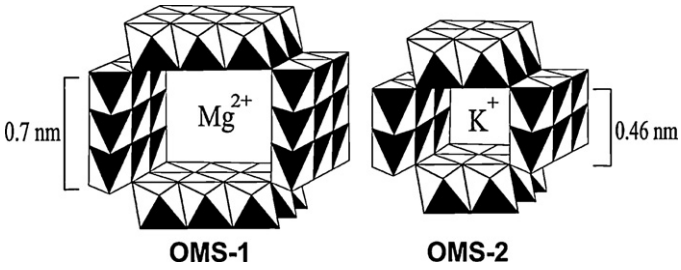

Fig. 1. Tunnel structure with the template ions of OMS materials.

is assumed to follow an ion exchange mechanism and the ion-exchange equilibrium is described using a non-ideal competitive adsorption (NICA) model [19]. Thus, the specifically bound amount, q_s, of protons and metal cations can be calculated from Eq. (1) [19], where κ and c are the affinity constant and the molar solution concentration. The parameter h depends on the binding stoichiometry and on the lateral interactions of the adsorbed species. The heterogeneity of the sites is characterized by the value p ($0 < p \leq 1$).

$$q_{sp,i} = q_{max}\left(\frac{h_i}{h_H}\right)\frac{(\kappa_i c_i)^{h_i}\left[\sum_j (\kappa_j c_j)^{h_j}\right]^{p-1}}{1+\left[\sum_j (\kappa_j c_j)^{h_j}\right]^{p}} \quad (i,j = \mathrm{H, Me}) \qquad (1)$$

It is assumed here that the maximum proton binding capacity is equal to the total amount of sites, q_{max}. Non-specific binding (q_b) is used to compensate the negative charge of the free sites and the bound cations are assumed to have the same equivalent ratios as in the bulk solution. The total bound amount of cation i is then $q_i = q_{sp,i} + q_{b,i}$. Invasion of anions in the nanopores is omitted.

Ion exchange is assumed to be the only mechanism for binding of cations other than manganese. As described in a previous paper [20], changes in the manganese oxide framework at low pH values must also be considered. Disproportionation of Mn^{3+} is assumed to take place according to $2Mn^{3+} \rightleftarrows Mn^{2+} + Mn^{4+}$. A vacancy (□) is also created when Mn^{2+} moves from the framework to the tunnel sites and becomes exchangeable. This process can be formally expressed by means of Eq. (2),

$$A_m^+(Mn_e^{3+}Mn_{1-e}^{4+}O_{\sim 2}) + \nu_H H^+ \overset{K_{dis}}{\rightleftarrows} A_n^+ Mn_r^{2+}(Mn_f^{3+}Mn_{1-r-f}^{4+}\square_r O_{\sim 2}) + (m-n)A^+ + 0.5\nu_H H_2O \qquad (2)$$

where K_{dis} is the apparent equilibrium constant. It is assumed that only a certain fraction of Mn^{3+} undergoes disproportionation and the above-mentioned stoichiometry gives $r = 0.5(e–f)$. A^+ represents an exchangeable univalent counter-ion and ν_H is considered as an adjustable parameter.

2.2. Kinetic model

Transport of ions in the tunnel-type manganese oxide microcrystals was described using the Nernst–Planck equation. No distinction was made between specifically and non-specifically bound species; only the overall values, q, were used for solid phase concentrations. In order to simplify calculation, the accumulation in the solid phase was evaluated using the approximate solution of Carta and Lewus [21]. In the approximate approach, the concentration profiles within the oxide particles are not calculated directly but the driving force is evaluated approximately from the difference between the surface and average concentrations. One-dimensional diffusion is assumed and in a system of N mobile ions,

the approximate expression for flux of ion i, J_i, can thus be given by Eq. (3).

$$J_i \approx -\frac{2z_i D_{m,i}}{\rho_s L}\frac{[\bar{q}_i - q_i^* \exp(z_i m/5)]}{1-\exp(z_i m/5)}m$$
$$\sum_{j=1}^{N} z_j^2 D_{m,j}\frac{[\bar{q}_j - q_j^* \exp(z_j m/5)]}{1-\exp(z_j m/5)} = 0 \quad (3)$$

D_m is the micro-crystalline diffusion coefficient, ρ_s is the material density, and z is the ion charge. Symbols with an over-bar and an asterisk represent the average and surface values, respectively. Assuming that external mass transfer resistance is negligible and that a local equilibrium is established at the particle surface, q_i^* is obtained from the equilibrium model described above. The parameter m is obtained from the condition of zero net current ($\Sigma z_j J_j = 0$) given in the second expression of Eq. (3) [21].

The crystals of both materials are taken as long hollow fibers which are open at both ends. The cylindrical walls of the crystals are considered impermeable, which means that ion diffusion in and out of the OMS fibers is only possible at the two ends. The mass balance for the batch system is shown in Eq. (4), where L is the average length of the crystals.

$$\frac{\partial \bar{q}_i}{\partial t} = -\frac{1}{\rho_s}\left(\frac{2}{L}J_i - \nu_i r_{dis}\right)$$
$$\frac{dc_i}{dt} = \frac{2V_s}{V_{liq}L}J_i$$
$$r_{dis} = k_{dis}\left[q_{Mn3+}^{\alpha} q_{H+}^{\beta} (q^{\circ})^{-(\alpha+\beta)} - \frac{1}{K_{dis}} q_{Mn2+}^{\gamma} (q^{\circ})^{-\gamma}\right] \quad (4)$$
$$K_{dis} = \frac{q_{Mn2+}}{q_{Mn3+}^2 q_{H+}^{\nu_H}} (q^{\circ})^{\nu_H+1}$$

Here, disproportionation of Mn^{3+} (see Eq. (2)) is accounted for by a simplified solid-phase reaction with a rate constant k_{dis} and an apparent equilibrium constant K_{dis}. The reaction orders were assumed to be equal to the stoichiometric coefficients; $\alpha = 2$, $\beta = \nu_H$ and $\gamma = 1$. The unit concentration (1 mol/kg) is given by q°.

2.3. Calculations

The NICA and kinetic parameters for OMS-1 were taken from an earlier publication [20]. Some readjustment was needed and the new values were found by trial-and-error. As noted earlier [20], the parameters are useful for correlation purposes only, and comparison of individual values is difficult. Because of the structural similarity of OMS-2, the same parameter values were used as the starting point and the new values were found using batch kinetic data.

The differential and arithmetic equations were solved numerically as described in [22]. The initial and boundary conditions for the batch kinetic calculations were as follows, where c^{init} refers to the initial concentration in the batch experiment.

$$t = 0 : c_i = c_i^{init}, \bar{q}_i = 0$$
$$t > 0, q_i^* = f(c_1, c_2 \ldots c_N)$$

3. Experimental

3.1. Synthesis of OMS-1 and OMS-2

The OMS-1 synthesis was adapted from the methods of Giovanoli et al. [7] and Feng et al. [23] and the details are reported elsewhere [20]. In brief, Na-buserite was first prepared by oxidizing freshly precipitated $Mn(OH)_2$ with O_2. Washed and centrifuged Na-buserite was converted to Mg-buserite by $MgCl_2$ solution (c_{Mg} = 1 mol/L) and then kept for 24 h under reflux. After refluxing, the solid was washed with deionized water and centrifuged.

OMS-2 was synthesized according to the method of DeGuzman et al. [24]. A synthetic raffinate solution, which contained 4500, 490, 300, 150, 200 and 3500 mg/L of Mn, Mg, Fe, Al, Ca and Na, respectively, was used as the manganese source [18]. The solution was acidified with concentrated HNO_3 and the oxidant, $KMnO_4$, was added. The mixture was refluxed for 24 h. The precipitate was separated and washed with deionized water until the effluent was free of acid. The solids were finally dried at 120 °C. The amount of $KMnO_4$ used in the original method was increased 1.5-fold in order to compensate for the oxidation of Fe(II) contained in the raffinate solution.

3.2. Characterization methods

The structure of the synthesized materials was analyzed using spectroscopic methods, scanning electron microscopy (SEM), N_2 adsorption measurements, and particle size measurements. Crystal structure and purity was verified by means of X-ray powder diffractometry (XRD, PANAnalytical X'Pert PRO and Phillips PW 1710 powder diffractometer with Cu K_α (0.154 nm) radiation). IR spectra were obtained using the standard KBr tablet method on a PerkinElmer 2000 FT-IR spectrometer. SEM images were taken using a JEOL JSM-5800 microscope equipped with an ultra dry X-ray detector from Thermo Fisher Scientific Inc. The particle size was analyzed by laser light scattering (Coulter LS130) with ultrasonic pretreatment.

The elemental composition of the synthesized material was analyzed from dissolved samples with plasma emission spectrometry (Iris Intrepid II XDL ICP-AES). In order to evaluate the accuracy of the analysis, some duplicate samples were made and analyzed. The error of analysis was estimated to be smaller than 5%. The average oxidation state (AOS) was measured as described elsewhere [20].

Uptake kinetics of metal cations (Cu^{2+}, Cd^{2+}, Mg^{2+} and Ca^{2+}) in the OMS-1 and (Cu^{2+}, Ni^{2+}, Mg^{2+}, Ca^{2+}, K^+ and Li^+) in the OMS-2 materials were determined at a constant supporting electrolyte concentration ($NaNO_3$, I_c = 0.1 mol/L). 0.5 g of dry material (in salt form) was weighed into a batch reactor. Total solution volume (V_{liq}) was 100 mL. Before addition of the metals, the OMS material dispersed in the background electrolyte solution was pre-equilibrated to pH 5. The metal uptake kinetics was measured by adding 2 mL of $Me(NO_3)_2$ solution with varying metal concentrations and measuring the solution concentration as a function of time. Solution pH was adjusted and kept at 5 by a pH-stat (Titralab TIM856, Radiometer). The adsorbed amount was calculated from the initial and equilibrium solution concentrations analyzed by means of ICP-AES. After the experiments the mass balance was checked by dissolving the washed and dried solid in acid and analyzing the metals with ICP-AES. The agreement was generally good, for example, the Cu balances were correct to within 5% in all cases.

4. Results

4.1. Material characterization

The synthesized materials were identified by comparing the XRD profiles and IR spectra with literature data. The XRD and IR spectra measured in this study for OMS-1 (Figs. 2 and 3) agree with those reported by Feng et al. [10,23,25]. In particular, the peak at 750 cm^{-1} is characteristic for OMS-1 [26,27]. It is also noteworthy that no extra peaks are found in the XRD profiles, indicating complete conversion during the hydrothermal treatment. The XRD profile of K-OMS-2 shown in Fig. 2 agrees well with reported data [24].

The chemical composition of the synthesized materials was estimated from the results of elemental analysis, thermal analysis, and

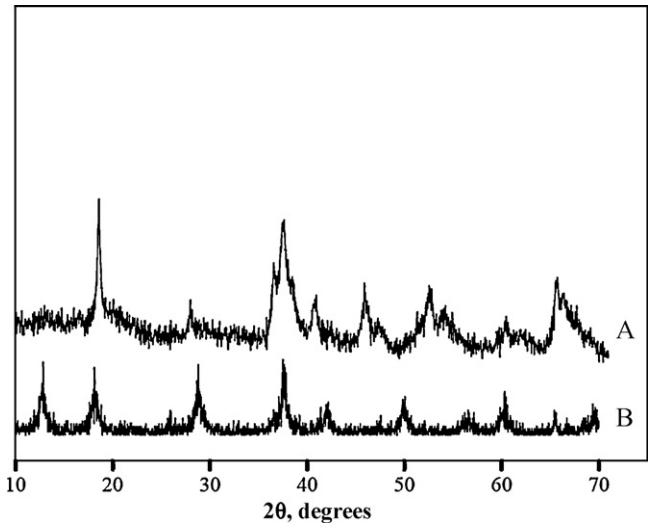

Fig. 2. XRD patterns of Mg-OMS-1 (A) and K-OMS-2 (B).

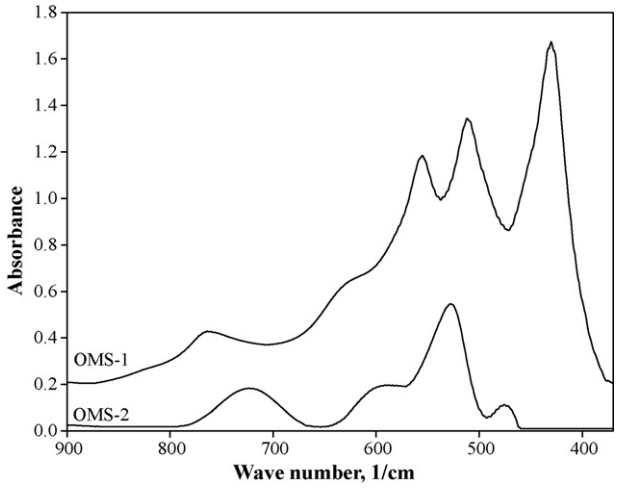

Fig. 3. FTIR spectra of studied OMS materials.

determination of the average manganese oxidation state (AOS). The average oxidation states of Mn in the synthesized materials were 3.8 for OMS-1 and 3.9 for OMS-2. If it is assumed that the manganese exists as Mn^{2+}, Mn^{3+} and Mn^{4+}, the structure of the materials after synthesis and gentle drying can be represented by the molecular formulas shown below [20]. The bracketed species refer to the oxide framework. As discussed later, only about half of the Mg ions contained in OMS-1 are exchangeable and the rest is assumed to be incorporated in the framework. The potassium ions in OMS-2 are all exchangeable.

$$Mg^{2+}_{0.08},\ Mn^{2+}_{0.022}\,[Mg^{2+}_{0.09}Mn^{3+}_{0.27}Mn^{4+}_{0.71}\square_{0.022}O_{\sim 2}]\cdot 2.0H_2O \quad \text{(OMS-1)}$$

$$K^{+}_{0.12},\ Mn^{2+}_{0.01}\,[Mn^{3+}_{0.2}Mn^{4+}_{0.8}\square_{0.023}O_{\sim 2}]\cdot 1.49H_2O \quad \text{(OMS-2)}$$

It can be seen in the calculated formulas that the amount of potassium in OMS-2 is close to the expected value (about 0.125 equiv/mol Mn [9,12,24]). The higher amount of Mg in OMS-1 (0.16 equiv/mol Mn) may be due to insufficient washing after synthesis. A small amount of Na remained in the structure of OMS-1 during synthesis but was neglected in the calculations. The molar ratio of oxygen to manganese was about two in both materials.

The shape of the OMS-1 crystals was a thin rod with an average length of 10 μm (see Fig. 4A). A slightly different crystal shape was found for OMS-2, as shown in Fig. 4B. In the calculations, the average length of the rod-like particles was taken as 10 μm for both materials. The thickness of both crystals was estimated as 0.2 μm.

Table 1
Equilibrium binding parameters of OMS-1 and OMS-2. $T = 25\ ^\circ C$.

OMS-1[a] $p = 0.2$ $K_{dis} = 3.0$ $\nu_H = 0.8$			OMS-2[b] $p = 0.2$ $K_{dis} = 1$ $\nu_H = 1.1$	
Ion	$\log\kappa$ (κ in L/mol)	h	$\log\kappa$ (κ in L/mol)	h
H^+	8.0	1.0	8.0	1.0
Na^+	1.0	1.0	1.0	1.0
Li^+	nd.	nd.	9.0	0.1
K^+	nd.	nd.	12	0.4
Mg^{2+}	5.0[b]	0.5[b]	0.7	0.02
Mn^{2+}	7.0	0.5	7.0	0.5
Cu^{2+}	36.7	0.15	28	0.21
Ni^{2+}	3.7[b]	0.16[b]	12	0.25
Cd^{2+}	12.5	0.4	nd.	nd.
Ca^{2+}	0	0.01	0	0.01

nd.: Not determined.
[a] Taken from Ref. [20].
[b] Estimated in this work.

4.2. Competitive sorption of metals

The acid-base properties and effect of solution pH on equilibrium metal binding in OMS-1 was studied previously and the parameter values given in Table 1 are taken from Ref. [20]. Except for the proton titration curve reported by Koivula et al. [18], similar data were not available for OMS-2 and the metal binding parame-

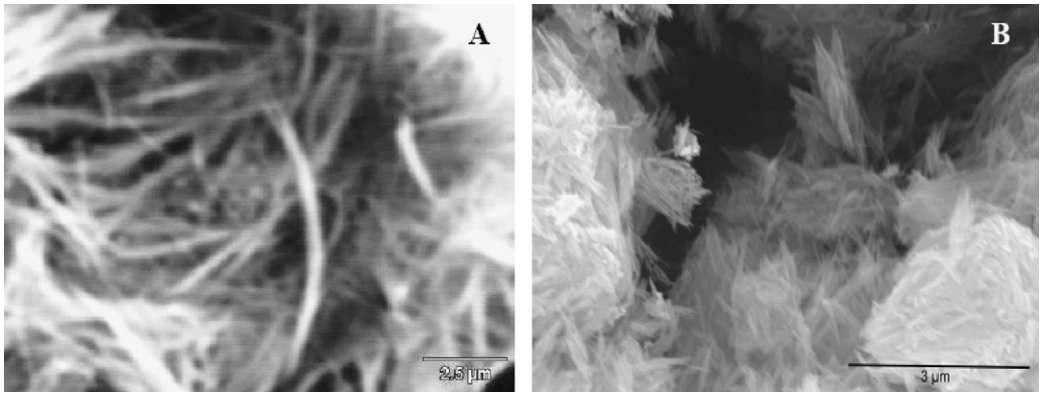

Fig. 4. SEM images Mg-OMS-1 (A) and K-OMS-2 (B).

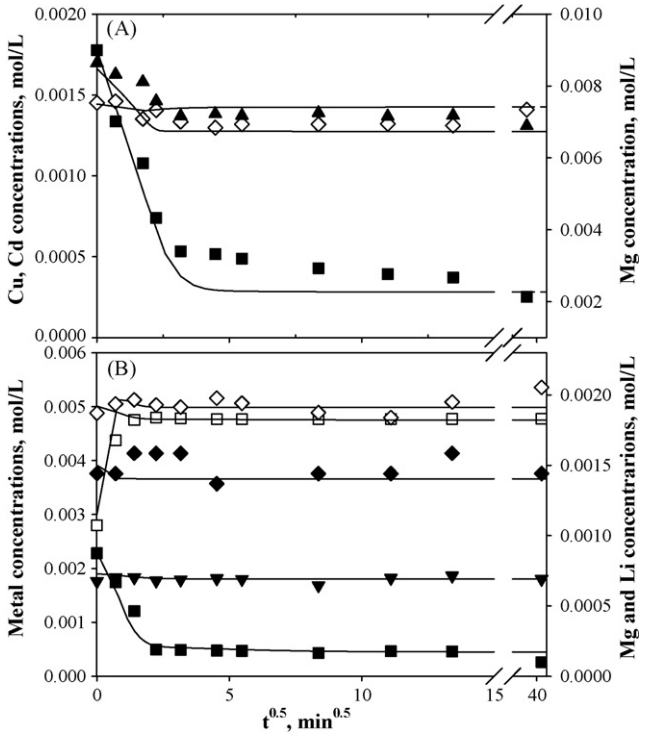

Fig. 5. Uptake kinetics of metals on OMS-1 (A) and OMS-2 (B). $T = 25\,^{\circ}C$, pH 5, $I_c = 0.1$ M ($NaNO_3$). Initial concentration of each metal was about 2 mmol/L, $c_{Ca}^{init} = 0$. Cu: filled squares, Ni: solid triangles down, Cd: solid triangles up, Mg: open diamonds, K: open squares and Li: solid diamonds. Solid lines were calculated from Eqs. (1)–(4) with the parameter values of Tables 1 and 2.

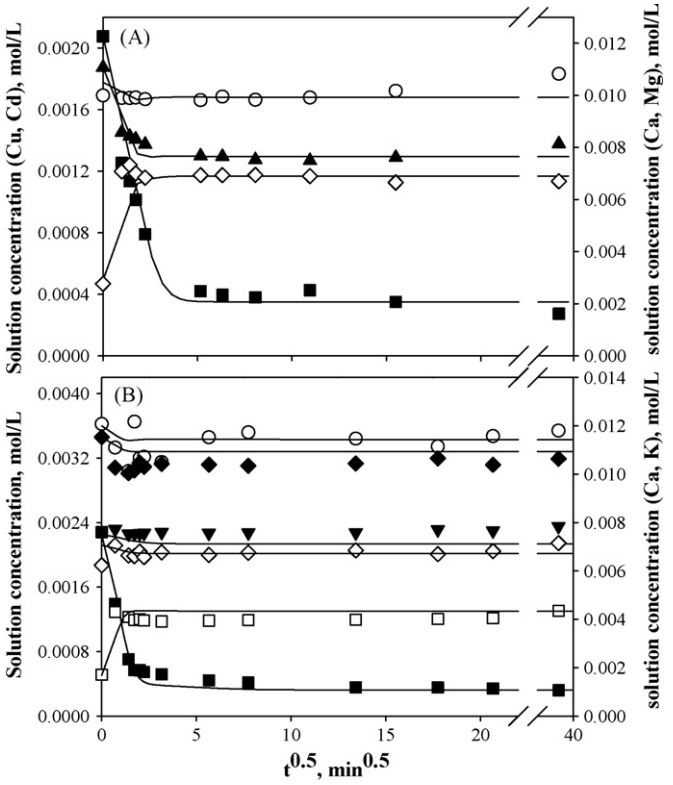

Fig. 6. Uptake kinetics of metals on OMS-1 (A) and OMS-2 (B). $T = 25\,^{\circ}C$, $I = 0.1$ M ($NaNO_3$). Initial concentration of each metal was 2 mM, $c_{Ca}^{init} = 10$ mM. The symbols correspond to metals: Cu is solid squares, Ni solid triangles down, Cd solid triangles up, Ca open circles, Mg open diamonds, K open squares, and Li solid diamonds. Solid lines were calculated from Eqs. (1)–(4) with the parameter values of Tables 1 and 2.

ters given in Table 1 were adjusted using the experimental results of this study.

According to the titration curves, both materials behave as weak acids and metal uptake with a reasonable capacity is possible at pH values above 3 [18,20]. Consequently, batch uptake measurements at pH 5 were used to get information on competitive sorption of metals and uptake rates. The metal concentrations of the model systems were chosen in such a way that the amounts of potentially interfering ions were similar to natural waters.

The system of metal uptake kinetics consists of partial exchange of the original counter-ions (Mg^{2+}, K^+ and Mn^{2+}) by H^+ and Na^+ during the pre-equilibration step and further exchange by the metal cations added in the solution. Therefore, the exchange processes in the case of OMS-1 and OMS-2 was followed by analysis of Mg and K concentrations. The experimental data are shown in Figs. 5–7. The concentration of desorbed and dissolved Mn was monitored but because the values were systematically very small (<1 mg/L), they are not shown. The experimental data were correlated with the batch kinetic model (Eqs. (1)–(4)) and the calculated values are shown as continuous lines. Because of uncertainties involved in determination of L, and to permit easier comparison between the materials, a lumped mass transfer parameter defined as $b_m = D_m/L^2$ was used. The estimated b_m values are given in Table 2. The value for H^+ was chosen quite arbitrarily since the calculated curves were found to be insensitive to this value.

The results shown in Figs. 5–7 indicate that both oxides have high affinity for copper even in the presence of Ca and Mg. If calcium was not added (Fig. 5), the Cu binding capacity of both materials was about 0.4 mmol/g when the solution concentration was 2 mmol/L. The Cu uptake measured in this study for OMS-1 was similar to the values measured by Eren et al. [6] for Pb and Balakhonov et al. [14] for Pb and Ba. The total number of ion-exchange sites estimated in this study was 2.3 mequiv/g for OMS-1 and 2.2 mequiv/g for OMS-2. The former value is the same as obtained earlier [20], while the latter markedly exceeds the value reported by Koivula et al. [18]. The higher exchange capacity of OMS-1 can be explained by the difference in site density, which can be estimated from the amounts of exchangeable ions in the studied materials. When applying the formulas given in Section 4.1, the number of exchangeable equivalents in the tunnel sites of OMS-1 is about 8% higher.

It is possible that steric exclusion from the narrower tunnel-system of OMS-2 results in a lower uptake capacity. The steric exclusion effects are not explicitly accounted for in the present model, although they can be represented formally by adjusting the parameter h in Eq. (1). The agreement between the calculated and experimental uptake curves was reasonably good when the initial copper concentration was 2 mmol/L.

Table 2
Mass transport parameter b_m for different cations in OMS-2 and OMS-1 at 25 °C.

Cation	b_m (10^{-3} s^{-1})	
	OMS-1	OMS-2
H^+	4	4
Na^+	0.8	0.6
Li^+	nd.	0.6
K^+	nd.	0.8
Mg^{2+}	0.7	0.3
Mn^{2+}	0.3	0.3
Cu^{2+}	0.15	0.15
Ni^{2+}	nd.	0.1
Cd^{2+}	0.5	nd.
Ca^{2+}	0.6	0.7

nd.: Not determined.

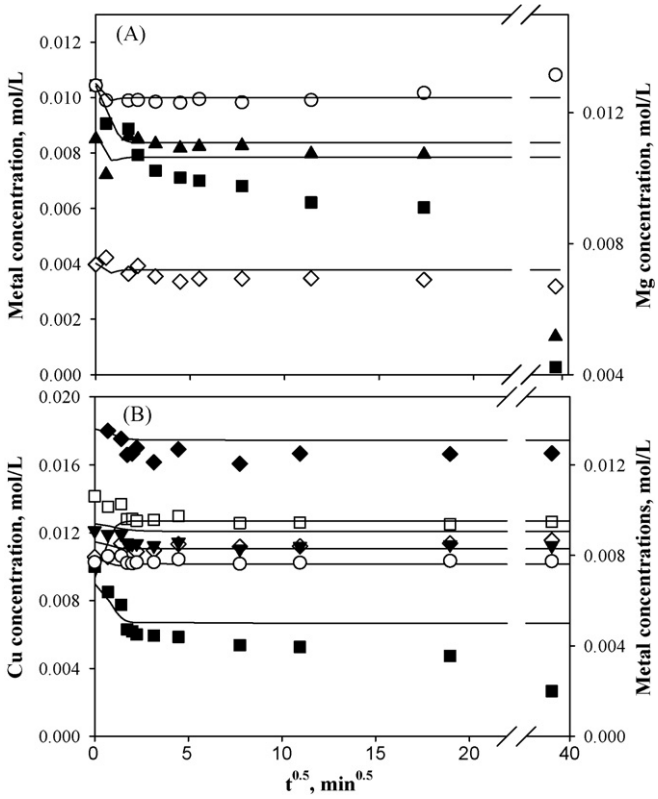

Fig. 7. Uptake kinetics of metals on OMS-1 (A) and OMS-2 (B). $T = 25\,^{\circ}C$, $I = 0.1$ M ($NaNO_3$). Initial concentration of each metal was 10 mM, $c_{Ca}^{init} = 10$ mM. The symbols correspond to metals: Cu is solid squares, Ni solid triangles down, Cd solid triangles up, Ca open circles, Mg open diamonds, K open squares and Li solid diamonds. Solid lines were calculated from Eqs. (1)–(4) with the parameter values of Tables 1 and 2.

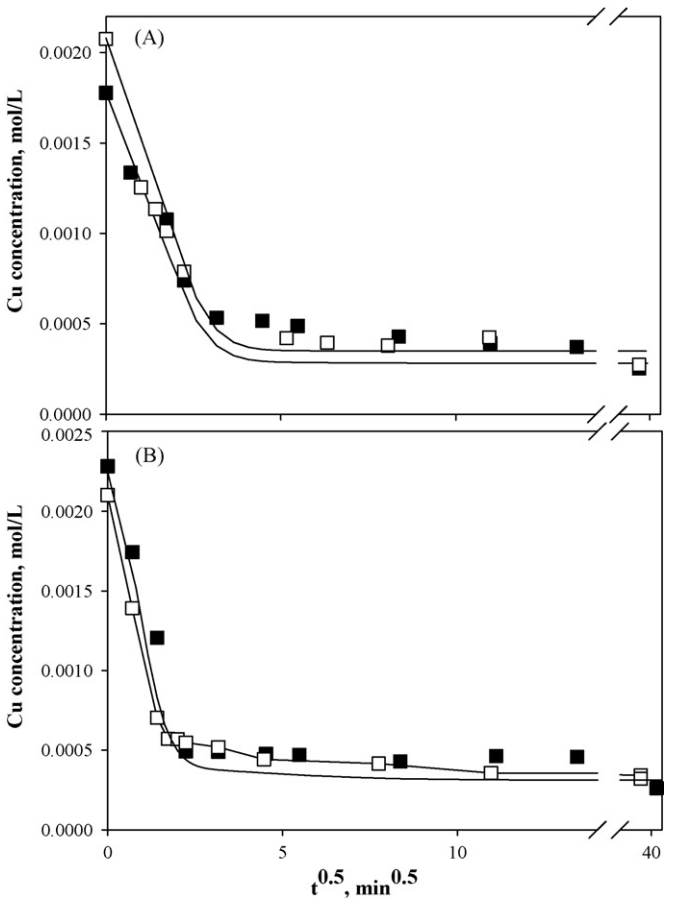

Fig. 8. Influence of calcium on copper uptake in OMS-1 (A) and OMS-2 (B). $T = 25\,^{\circ}C$, $I = 0.1$ M ($NaNO_3$). $c_{Cu}^{init} = 2$ mmol/L, $c_{Ca}^{init} = 0$ (filled symbols), 10 mmol/L (open symbols).

However, when the more concentrated ($c_{Cu}^{init} = 10$ mmol/L) solution was used (Fig. 7) the final Cu uptake in both materials (1.3 mmol/g for OMS-2 and 0.9 mmol/g for OMS-1) was much higher than predicted by the model. Moreover, the shape of the uptake curves suggests that besides the normal ion exchange, there is another slower mechanism, which becomes important at higher solution concentrations. A similar trend was also found by Eren et al. [6] with MnO_2 materials and they explained it by assuming two different sites with different adsorption energies and affinities. The influence of low affinity sites can be seen only in more concentrated solutions (Fig. 7).

As discussed above, metal uptake is assumed to take place by displacement of the proton, Na^+ and the original counter-ions from the charged tunnel sites of the OMS framework. A small contribution of Mn^{3+} dissolution according to Eq. (2) is also present and this effect explains the curve shapes at low metal concentrations. It is known [9] that some transition metals can be incorporated in the OMS structure by replacement of manganese ions or filling of the vacant octahedra. No data are available on the rate of this process but it is expected to be much slower than ion exchange in the tunnel sites. In principle, the slow depletion from the solution can also stem from copper precipitation but this possibility can be ruled out because the solubility limit at the experimental conditions is about 20 mmol/L, as shown by separate measurements.

Uptake of Cd in OMS-1 and Ni in OMS-2 was much smaller when compared with Cu indicating a much weaker affinity. Analogous to copper, the values of the *h* parameters estimated for Ni and Cd suggest strong steric exclusion from the tunnel sites of both materials. Moreover, the selectivity of OMS-2 for monovalent cations (K and Li) was much smaller than for Cu, but clearly higher than for Mg. The shape and size of the nanopores in OMS-2 formed with K as a template ion obviously favors alkali metals over alkaline earth metals. It seems that the selectivity of OMS-2 for Ni over Ca and Mg could be sufficient for uses such as radio nuclide capture in natural systems, where the metal concentrations are usually very low [28]. More experiments at the correct concentration range are, however, needed to verify this possibility.

The influence of Ca on copper exchange is further clarified in Fig. 8. Obviously, the presence of Ca in the metal solution has an only insignificant effect on the equilibrium Cu uptake or on the uptake kinetics due to the huge difference in the affinities (see Table 1) in the studied concentration range. A similar trend was observed for other metals (Ni, Cd, K and Li (not shown here)) and this supports the assumption that the studied materials are capable of adsorbing harmful metal ions from natural waters rich in Ca and Mg. However, only about half of Mg^{2+} (in OMS-1) and K^+ (in OMS-2) present initially in the OMS structure were displaced by the transition metal cations. This indicates that the second half of the template ions inserted in the synthesis is not exchangeable, possibly due to steric hindrances or incorporation in the Mn octahedra.

In summary, all the uptake curves are characterized by a rapid initial part accompanied in some cases by a slow change in the solution concentration. The fast part having a half-time of a few minutes is interpreted as exchange of the cations in the tunnel sites. As shown in Table 2, the cation diffusion parameters are similar in OMS-1 and OMS-2 crystals and no significant effect of tunnel size on the diffusion rates can be observed. The slow part of the curves cannot be described adequately by the present model and its origin remains unclear, as discussed above.

5. Conclusions

Two tunnel-structure manganese oxides OMS-1 and OMS-2 were synthesized and characterized. The materials were tested for competitive uptake from mixed metals solution and for uptake kinetics. The experimental data were correlated using the NICA equilibrium model and the Nernst–Planck equation for ion transport in the solids.

The results of batch uptake experiments indicate that both oxides have high affinity for copper. Moreover, removal of copper from mixed metal solutions at pH 5 is not affected by Ca^{2+} or Mg^{2+} at concentrations typically found in natural waters. In a similar way, cadmium was bound on OMS-1 and Ni on OMS-2 at the studied conditions but the uptake capacities were much smaller than for Cu. Reasonable exchange rates can be attained because of the small particle dimensions. The results show that both materials are promising for environmental applications in which harmful metal ions should be removed from a waste stream, for example, from mine effluents. Before being suitable for industrial use, the material must, however, be transformed from finely divided powder to a practically useful form.

Acknowledgements

Financial support from the Academy of Finland ("Sustainable Production and Products"-programme) is gratefully acknowledged. The authors also thank Ms. Anne Hyrkkänen for assistance in experimental and analytical work.

References

[1] D.B. Johnson, K.B. Hallberg, Acid mine drainage remediation options: a review, Sci. Total Environ. 338 (2005) 3–14.
[2] Y.-L. Jan, S.-C. Tsai, C.-N. Hsu, Assiciating characterization of bentonite-based buffer/backfill materials by distribution ratio (R_d) and (plastic index (PI), J. Marine Sci. Technol. 15 (1) (2007) 17–23.
[3] D. Arcos, F. Grandia, C. Domènech, A.M. Fernández, M.V. Villar, A. Muurinen, T. Carlsson, P. Sellin, P. Hernán, Long-term geochemical evolution of the near field repository: insights from reactive transport modelling and experimental evidences, J. Contam. Hydrol. 102 (2008) 196–209.
[4] M. Fall, J.C. Célestin, F.S. Han, Suitability of bentonite-paste tailings mixture as engineering barrier material for mine waste containment facilities, Miner. Eng. 22 (2009) 840–848.
[5] E. Eren, B. Afsin, An investigation of Cu(II) adsorption by raw and acid-activated bentonite: a combined potentiometric, thermometric, XRD, IR DTA, J. Hazard. Mater. 151 (2008) 682–691.
[6] E. Eren, B. Afsin, Y. Onal, Removal of lead ions by acid activated and manganese oxide-coated bentonite, J. Hazard. Mater. 161 (2009) 677–685.
[7] R. Giovanoli, E. Stähli, W. Feitknecht, Über Oxidhydroxide des vierwertigen Mangans mit Schichtengitter Natriummangan(II,III) manganat(IV), 1.Mitteilung, Helv. Chim. Acta 53 (1970) 209–220 (in German).
[8] M. Tsuji, M. Abe, Synthetic inorganic ion-exchange materials. XXXVIII. Acid-base properties of a cryptomelane-type hydrous manganese(IV) oxide and some chromatographic applications, Bull. Chem. Soc. Japan 58 (4) (1985) 1109–1114.
[9] Q. Feng, H. Kanoh, K. Ooi, Manganese oxide porous crystals, J. Mater. Chem. 9 (1999) 319–333.
[10] X.H. Feng, W.F. Tan, F. Liu, J.B. Wang, H.D. Ruan, Synthesis of todorokite at atmospheric pressure, Chem. Mater. 16 (2004) 4330–4336.
[11] S. Ching, K.S. Krukowska, S.L. Suib, A new synthetic route to todorokite-type manganese oxides, Inorg. Chim. Acta 294 (1999) 123–132.
[12] M. Tsuji, Pb^{2+} separation from concentrated electrolyte solutions by a cryptomelane-type manganic acid and titanium antimonic acid, Solvent Extract. Ion Exchange 19 (3) (2001) 531–551.
[13] N. Das, R.K. Jana, Adsorption of some bivalent heavy metal ions from aqueous solutions by manganese nodule leached residues, J. Colloid Interface Sci. 293 (2006) 253–262.
[14] S.V. Balakhonov, B.R. Churagulov, E.A. Gudilin, Selective cleaning of ions of heavy metals from water solutions using the H-form of todorokite synthesized by the hydrothermal method, J. Surf. Invest., X-ray, Synchrotron Neutron Tech. 2 (1) (2008) 152–155.
[15] X.H. Feng, L.M. Zhai, W.F. Tan, F. Liu, J.Z. He, Adsorption and redox reactions of heavy metals on synthesized Mn oxide minerals, Environ. Pollut. 147 (2007) 366–373.
[16] H.-J. Fan, P.R. Anderson, Copper and cadmium removal by Mn oxide-coated granular activated carbon, Sep. Purif. Technol. 45 (2005) 61–67.
[17] A. Dyer, M. Pillinger, J. Newton, R. Harjula, T. Möller, S. Amin, Sorption behaviour of radionuclides on crystalline synthetic tunnel manganese oxides, Chem. Mater. 12 (2000) 3798–3804.
[18] R. Koivula, J. Pakarinen, M. Sivenius, K. Sirola, R. Harjula, E. Paatero, Use of hydrometallurgical waste water as a precursor for the synthesis of cryptomelane-type manganese dioxide ion exchange material, Sep. Purif. Technol. 70 (1) (2009) 53–57.
[19] D.G. Kinniburgh, H. van Riemsdijk, L.K. Koopal, M. Borkovec, M.F. Benedetti, M.J. Avena, Ion binding to natural organic matter: competition, heterogeneity, stoichiometry and thermodynamic consistency, Colloids Surf. A 151 (1999) 147–166.
[20] J. Pakarinen, M. Laatikainen, K. Sirola, E. Paatero, R. Koivula, R. Harjula, Behavior of silica-supported manganese oxides in hydrometallurgical separations, Sep. Sci. Technol. 44 (2009) 3045–3074.
[21] G. Carta, R.K. Lewus, Film model approximation for particle-diffusion-controlled multicomponent ion exchange, Sep. Sci. Technol. 34 (1999) 2685–2697.
[22] K. Sirola, M. Laatikainen, M. Lahtinen, E. Paatero, Separation of copper and nickel from concentrated $znso_4$ solutions with silica-supported chelating adsorbents, Sep. Purif. Technol. 64 (2008) 88–100.
[23] X.H. Feng, F. Liu, W.F. Tan, X.W. Liu, Synthesis of birnessite from the oxidation of Mn^{2+} by O_2 in alkali medium: effects of synthesis conditions, Clays Clay Miner. 52 (2) (2004) 240–250.
[24] R.N. DeGuzman, Y.-F. Shen, E.J. Neth, S.L. Suib, C.-L. O'Young, S. Levine, J.M. Newsam, Synthesis and characterization of octahedral molecular sieves (OMS-2) having the hollandite structure, Chem. Mater. 6 (1994) 815–821.
[25] Z.-R. Tian, Y.-G. Yin, S.L. Suib, Effects of Mg^{2+} ions on the formation of todorokite type manganese oxide octahedral molecular sieves, Chem. Mater. 9 (1997) 1126–1133.
[26] F.A. Al-Sagheer, M.I. Zaki, Synthesis and surface characterization of OMS-1-type microporous manganese oxides: implications for shape-selective oxidation catalysts, Micropor. Mesopor. Mater. 67 (2004) 43–52.
[27] R.M. Potter, G.R. Rossman, The tetravalent manganese oxides: identification, hydration, and structural relationships by infrared spectroscopy, Am. Miner. 64 (1979) 1199–1218.
[28] A. Dyer, M. Pillinger, J. Newton, R. Harjula, T. Möller, S. Amin, Sorption behavior of radionuclides on crystalline synthetic tunnel manganese oxides, Chem. Mater. 12 (2000) 3798–3804.